RSC Advances

PAPER

View Article Online
View Journal | View Issue

Cite this: *RSC Adv.*, 2025, **15**, 24802

Oxygen vacancies mediated enhanced photocatalytic activity of band gap engineered $BaSn_{1-x}Cu_xO_3$ towards methylene blue degradation under visible and sunlight†

Suruthi Rajendran and R. Vijayaraghavan *

Photocatalysis, an advanced oxidation process (AOP), has been well explored as a promising and sustainable technology for tackling environmental pollution. This method involves semiconductors which generate powerful reactive oxygen species, capable of breaking down organic pollutants, on excitation with appropriate light energy. Among the diverse range of oxide semiconductors explored, perovskite oxides are an important family. While $BaSnO_3$ is a known perovskite photocatalyst, its intrinsic photocatalytic efficiency is limited by poor separation of charge carriers. To overcome this, a proven strategy is to create oxygen vacancies. These defects suppress electron–hole recombination leading to enhanced photocatalytic degradation. Hence, we have synthesized the system $BaSn_{1-x}Cu_xO_3$ (x = 0.0 to 0.2) and characterized well. Synthesis of the $BaSn_{1-x}Cu_xO_3$ series was successfully carried out *via* a facile solid-state reaction route. Powder X-ray diffraction (XRD) confirms the phase purity and cubic crystal structure. Fourier transform infrared spectroscopy (FT-IR) confirms the Ba–O, Sn–O, Cu–O vibrations. The surface morphology and particle size distribution examined using field emission scanning electron microscopy (FE-SEM) reveal that the particles are cubic in shape. The optical properties investigated using ultraviolet diffuse reflectance spectroscopy (UV-DRS) indicate the band gaps to be in the range of 3.15–2.42 eV. Photoluminescence study confirms the effective charge carrier separation on doping with Cu. Its photocatalytic activity under visible and sunlight using methylene blue (MB) as a model pollutant has been studied. Indeed, we could enhance the photocatalytic activity of $BaSnO_3$ and Cu doping at the Sn site (x = 0.2) exhibits 8 times higher rate constant than the parent phase under visible light and 60 times higher under sunlight respectively. The degradation percentages of MB are more than 95% in the doped phase in 30 min in both visible & sunlight whereas the parent phase exhibits it in 3 h. The significantly enhanced activity can be attributed to the oxygen vacancies created due to the substitution of Sn^{4+} by Cu^{2+}. We have also proposed a possible degradation pathway. This study constitutes the first documentation of the photocatalytic activity of $BaSn_{1-x}Cu_xO_3$, thereby opening new avenues for its potential applications in environmental remediation.

Received 25th April 2025
Accepted 9th July 2025

DOI: 10.1039/d5ra02900g

rsc.li/rsc-advances

1 Introduction

The treatment of organic matter in wastewater has become the focus of attention in environmental remediation. With the rapid development of industry and agriculture, serious water pollution results from the emission of many organic pollutants.[1–4] Synthetic dyes, including methylene blue (MB), widely used in industries like textiles, pose significant health risks. These risks include carcinogenic effects, mutagenicity, dermatological issues, and other serious health problems.[5–12] The most popular techniques for eliminating contaminants include chemical, biological, and physical adsorption techniques.[13–15] In recent years, there has been a lot of interest in heterogeneous photocatalytic destruction of refractory organic contaminants from water by semiconductors.[16,17] Perovskite-type semiconductor oxides have garnered significant interest for their photocatalytic properties, driven by their cost-effectiveness, exceptional catalytic performance, and environmental compatibility.[18–20] The perovskite oxides of the general formula, ABO_3, formed between the oxides of alkaline-earth metals (A = Ca, Sr, and Ba) and those of the group IV elements are of great industrial and technological importance. For photocatalytic pollutant degradation, a range of perovskite materials have been investigated, including, $ASnO_3$ (A = Ca, Sr, Ba), $LaCoO_3$, $BaZrO_3$, and $LaNiO_3$. Among these, $BaSnO_3$,

Department of Chemistry, School of Advanced Sciences, Vellore Institute of Technology, Vellore 632 014, India. E-mail: rvijayaraghavan@vit.ac.in

† Electronic supplementary information (ESI) available. See DOI: https://doi.org/10.1039/d5ra02900g

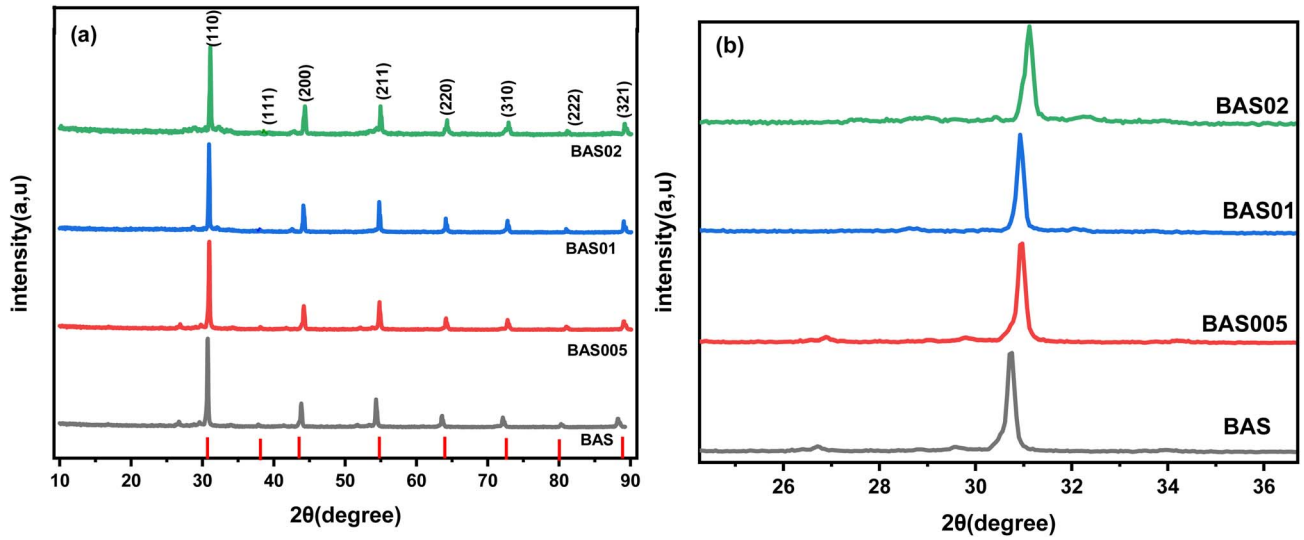

Fig. 1 (a) XRD patterns of BAS, BAS005, BAS01, BAS02 (b) Gaussian curve.

Table 1 Lattice parameter and strain of $BaSn_{1-x}Cu_xO_3$

Composition x	Lattice parameter (Å)	Strain $\times 10^{-3}$
0.0	4.116(3)	0.86
0.05	4.012(3)	1.27
0.10	3.934(5)	1.66
0.20	3.728(8)	4.32

a simple cubic perovskite, is an electrical insulator characterized by a wide band gap of 3.1 eV.[21,22] Properties of $BaSnO_3$ have been modified by heterovalent substitutions both at Ba site (La^{3+}) and Sn site (Nb^{5+}, Ni^{2+}, Cr^{3+}, Mn^{3+}, Sb^{5+}, Fe^{3+}) and studied for its magnetic, electrical properties.[23–29] Fe^{3+} substitution[30] only has been studied for its photocatalytic activity (for dye degradation) and it exhibits a degradation of 93% in 4 h which is much lower than the present study of Cu^{2+} substitution. Cu^{2+} substituted $BaSnO_3$ has not yet been studied for its photocatalytic activity and it is expected to enhance the performance due to oxygen vacancies created.

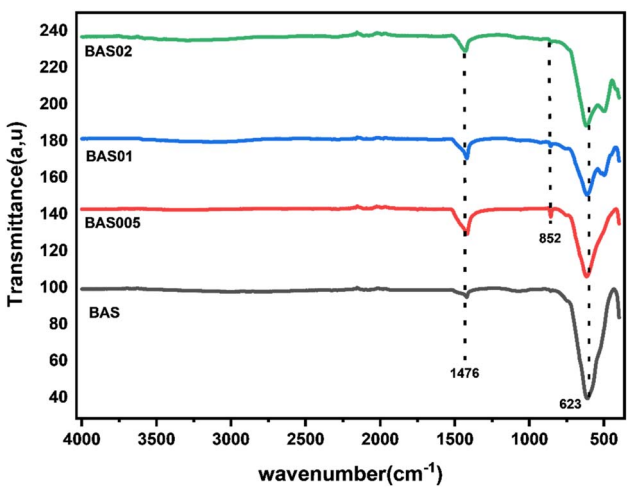

Fig. 2 FT-IR spectra of BAS, BAS005, BAS01, BAS02.

$BaSnO_3$'s outstanding optoelectronic characteristics, strong electron mobility, and appropriate energy band alignment make it a promising material for photocatalytic applications. However, the high charge carrier recombination rate and low visible-light absorption range limit the visible-light photocatalytic efficiency of $BaSnO_3$.[31] To deal with these challenges, various strategies[32–34] as heterojunction formation, morphology control, and defect engineering (*e.g.*, doping and oxygen vacancies) have been adopted to enhance its performance.[35] Introducing oxygen vacancies (OVs) is a proven strategy for enhancing photocatalyst performance.[36,37] These defects modify the catalyst's electrical and chemical properties at the molecular level, leading to improved activity. Oxygen vacancies are crucial for photocatalysis. These defects in the material's structure affect its electronic properties, charges movement within it, and surface reactivity. All of these factors are essential for efficient light absorption and the catalytic reactions that drive photocatalysis.[38]

In this work, we present Cu-doped $BaSnO_3$ with oxygen vacancies as an efficient photocatalyst for degrading MB dye under visible and sunlight. The Cu doping and associated oxygen vacancies in $BaSnO_3$ enhance visible light absorption, improve charge carrier separation, and boost surface reaction kinetics. The synthesized Cu-doped $BaSnO_3$ with oxygen vacancies exhibit significant degradation of MB dye under both visible and sunlight irradiation, making them a potential candidate for practical applications in wastewater treatment. The findings of this study will contribute to the development of efficient and sustainable photocatalytic technologies for environmental remediation.

2 Experimental section

2.1 Materials

The chemicals used for the synthesis of Cu-doped $BaSnO_3$ nanoparticles are as follows; barium carbonate ($BaCO_3$, 99%) copper oxide (CuO, 99%), and tin oxide (SnO_2, 99%) were procured from SD fine chemicals methylene blue ($C_{16}H_{18}ClN_3S$), were purchased from SRL Chemicals and used as received without any further purification.

2.2 Synthesis of Cu-doped barium stannate

Solid-state ceramic method was employed to prepare $BaSn_{1-x}Cu_xO_3$ (x = 0.0 to 0.2) powder. Stoichiometric amounts of barium carbonate ($BaCO_3$), tin oxide (SnO_2), and cupric oxide (CuO) were mixed in an agate motor. The homogeneous mixture thus obtained was heated in an alumina crucible to a temperature of 1200 °C for 24 h with intermittent grindings. $BaSnO_3$ is named BAS, $BaSn_{0.95}Cu_{0.05}O_3$ as BAS005, and $BaSn_{0.9}Cu_{0.1}O_3$ as BAS01, $BaSn_{0.8}Cu_{0.2}O_3$ as BAS02.

2.3 Photocatalytic experiment

The appropriate amount of the catalyst was suspended in 50 ml of the dye (methylene blue) solution. Before light irradiation, the suspension of the photocatalyst with the pollutant solution was kept in the dark for 30 min to attain adsorption–desorption equilibrium. 18 W UV-low pressure (mercury filament) lamp 18 W cm^{-2}/254 nm was used as an ultraviolet light source for BAS. A 500 W visible lamp (tungsten) 500 W cm^{-2} was used as a light source for BAS005, BAS01, BAS02, to degrade the pollutant. At regular time intervals, a 2 ml sample was collected and centrifuged at 4000 rpm. The absorbance of the supernatant liquid was analyzed by an ultraviolet-visible spectrophotometer (JASCO V-730) at an appropriate wavelength for degradation studies. The same procedure was carried out for pollutant degradation in an ambient sunlight experiment conducted at Vellore Institute of Technology, Vellore (latitude 12.970565; longitude 79.159484) in Tamil Nadu, India.

$$\text{Degradation efficiency (\%)} = [(C_0 - C_t)/C_0] \times 100 \quad (1)$$

where, C_0 and C_t were the concentrations of the pollutant at the initial time and certain time, respectively.

2.4 Characterization of $BaSn_{1-x}Cu_xO_3$

The synthesized $BaSn_{1-x}Cu_xO_3$ product was characterized by powder X-ray diffraction (XRD) using PANalytical X'Pert3 with

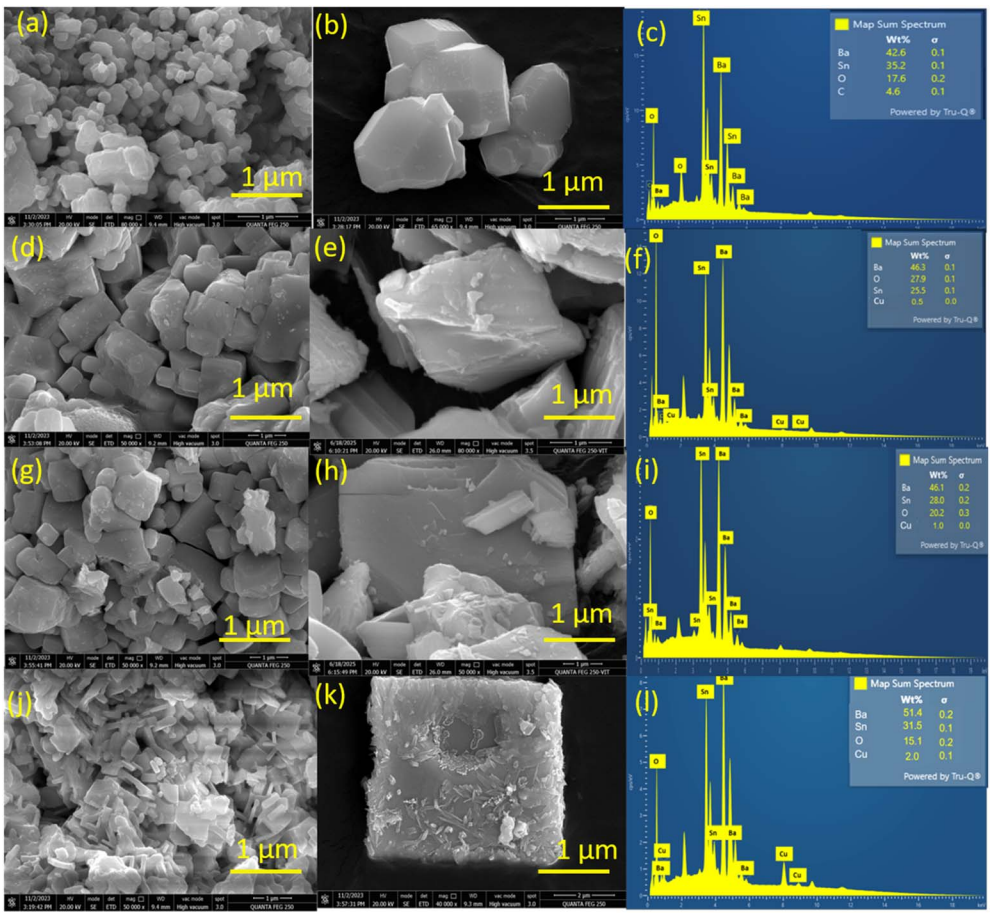

Fig. 3 (a and b) FESEM image of BAS, (c) EDAX of BAS, (d and e) FESEM image of BAS005, (f) EDAX of BAS005, (g and h) FESEM image of BAS01, (i) EDAX of BAS01, (j and k) FESEM image of BAS02, (l) EDAX of BAS02.

Cu K_α radiation (λ = 1.5406 Å). The surface morphology and elemental mapping for $BaSn_{1-x}Cu_xO_3$ were studied using Thermo Fisher FEI QUANTA 250 (FESEM) equipped with an energy-dispersive X-ray analysis unit operating at 30 kV. The X-ray photoelectron spectroscopy (XPS) were recorded using a Thermo Scientific K-Alpha X-ray Photoelectron Spectrometer System. Fourier transform infrared (FT-IR) spectra were studied using a Thermo Scientific (Nicolect iS10) spectrometer. The bandgap and degradation process were analyzed using a UV-visible-NIR spectrophotometer (JASCO V-670). USA. High-resolution mass Spectra (HR-MS) were recorded using a Waters – XEVO G2-XS-QToF mass spectrometer (sequence of measurements).

3 Results and discussion

3.1 Structural and morphological characterization of $BaSn_{1-x}Cu_xO_3$

3.1.1 X-ray diffraction. The X-ray diffraction patterns (Fig. 1(a)) of the synthesized products, confirm the single phase formation of $BaSn_{1-x}Cu_xO_3$ up to x = 0.2. The obtained diffraction peaks observed for the pristine $BaSnO_3$ at 2θ values of 30.85, 38.06, 44.16, 54.63, 64.12, and 72.85° can be indexed to the (110), (111), (200), (211), and (310) diffraction planes, conforming to the JCPDS data card (no. 15-0780). Fig. 1(a) confirms the formation of single-phase $BaSnO_3$ with a perovskite structure and the successful incorporation of Cu without altering the crystal structure.[39,40] Though we expect a slight increase of lattice parameter with Cu doping, the decrease in lattice parameter (Fig. 1(b), and Table 1) with increase in Cu doping can be attributed to the partial disorder of Cu at Ba site, in the crystal lattice. Earlier literature of Cu substituted $BaSnO_3$ reports Cu substitution at Ba Site.[41–43] There have been earlier reports on grain growth during the synthesis process upon substitution.[44–49]

The lattice strain calculated using Williamson–Hall plot is given in Table 1. The strain increases with increase in Cu^{2+} substitution.[50]

3.2 FTIR analysis

The FTIR spectra of the pure $BaSnO_3$ and Cu-doped $BaSnO_3$ samples measured in the range 4000–400 cm^{-1} are shown in (Fig. 2). The IR spectra absorption band below 1000 cm^{-1} correspond to the deformation modes of Sn–O bonds in SnO_6

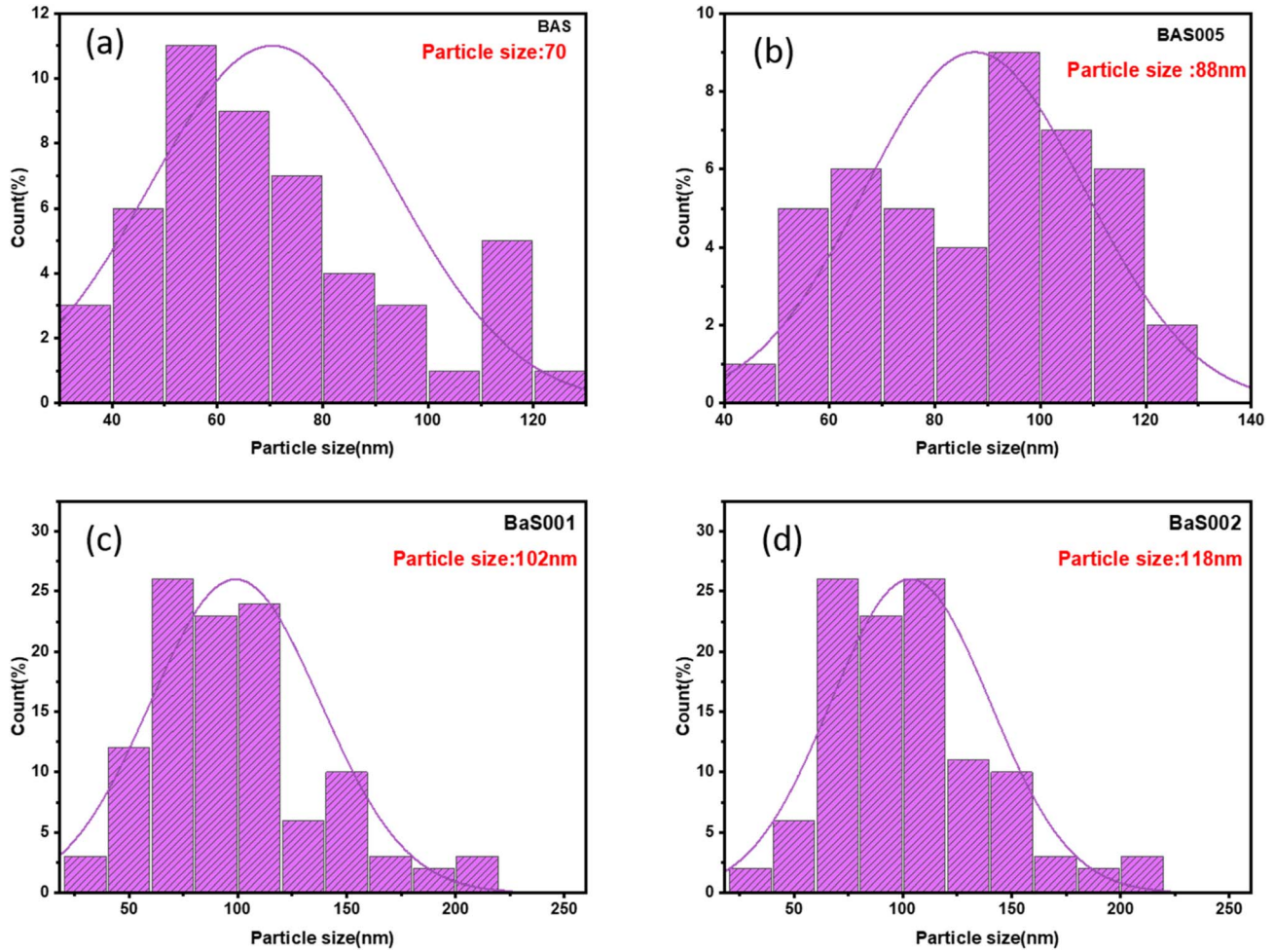

Fig. 4 Calculated histogram for particle size of (a) BAS and (b) BAS005 (c) BAS01 (d) BAS02.

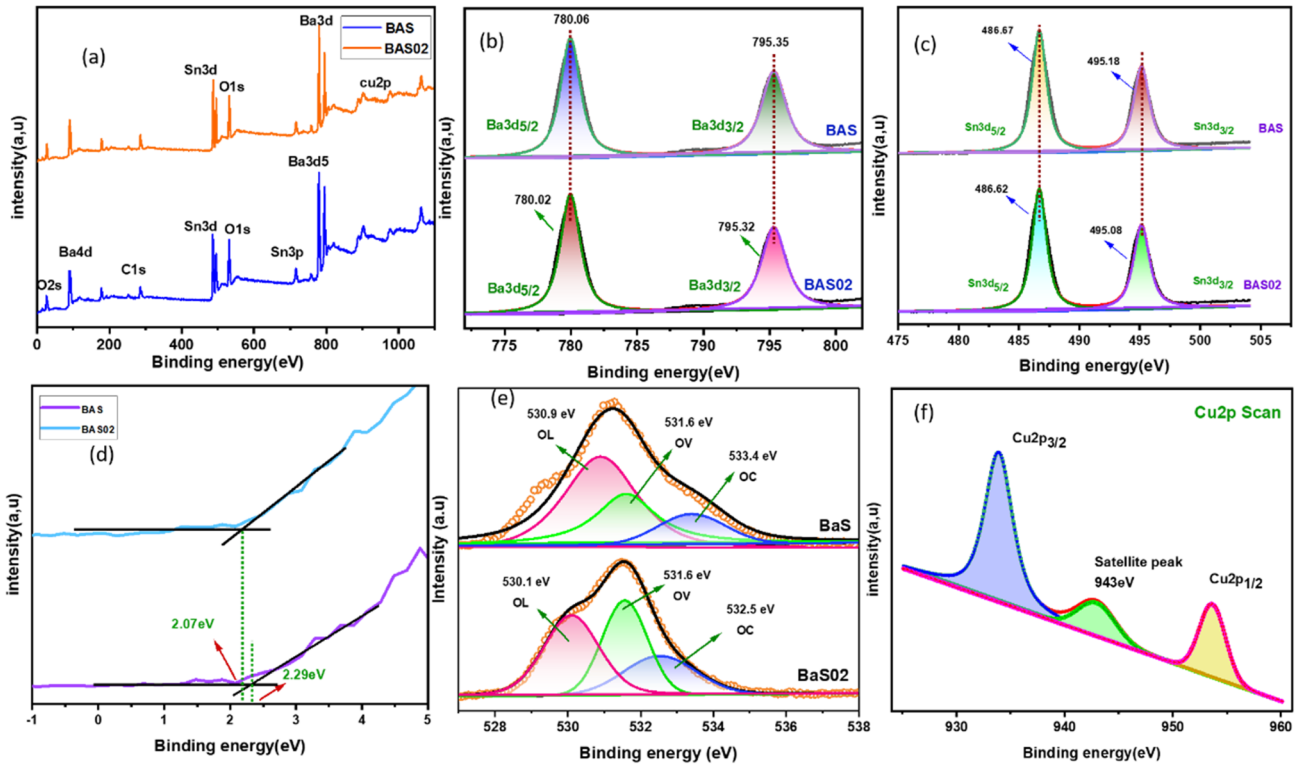

Fig. 5 XPS analysis of pure BAS and BAS02 powder sample (a). XPS survey spectrum Of BAS and BAS02 (b). Core level splitting of peaks of Ba (c). The core level splitting of peaks of Sn (d). Valance band of BAS and BAS02 (e). Core level splitting of peaks of O and (f) core level splitting of peaks of Cu 2p.

octahedra[51] and 1476 cm^{-1} which pertains Ba–O vibrations.[52] The Cu–O stretching vibration, observed at 852 cm^{-1}, appears only in the Cu-doped sample.

3.3 FE-SEM analysis of $BaSn_{1-x}Cu_xO_3$

Field Emission-Scanning Electron Microscope (FE-SEM) analysis was employed to characterize the morphologies of synthesized photocatalysts.[53,54] Fig. 3 show the FE-SEM images and elemental compositions of pure and Cu substituted $BaSnO_3$. It indicates cuboidal shape of the particles in general. With increase in Cu doping, the cuboidal shape is more regular with its size increasing. The surface roughness seems to increase on going from 0.0 composition to 0.2 composition.[53–55] The atomic percentages of the elements present in the catalysts on the basis of FESEM analysis are for BAS Ba = 18.2%, Sn = 17.44%, and O = 64.70, BAS005 Ba = 15.3% Sn = 10.83% O = 73.44%, Cu =

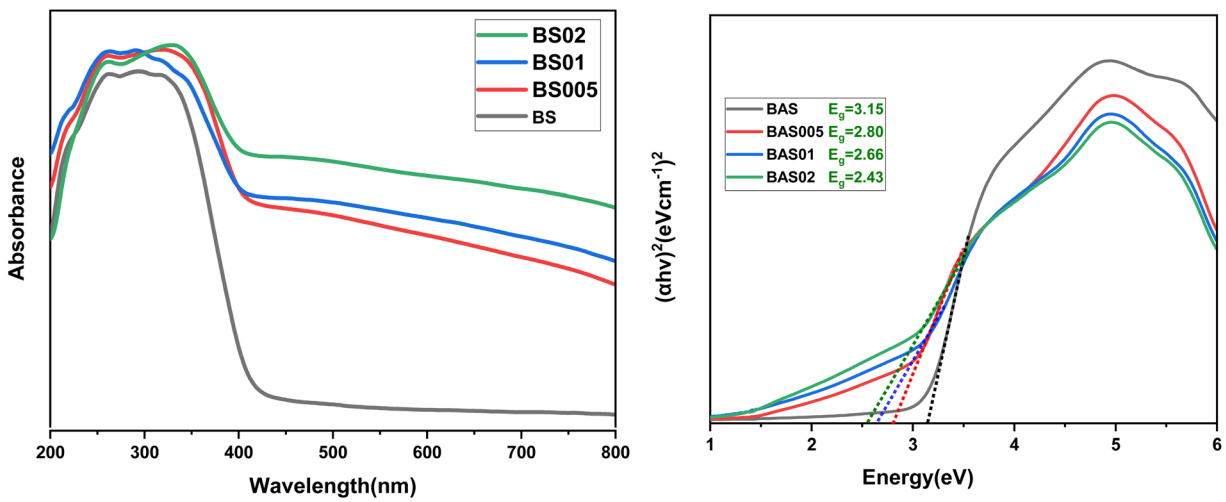

Fig. 6 UV-DRS reflectance spectra and Tauc plot of Cu-doped $BaSnO_3$.

0.8%, and BAS01, Ba = 18.31%, Sn = 12.80%, O = 67.80%, Cu = 1.8% and BAS02, Ba = 19.22%, Sn = 18.38%, O = 60.2%, Cu = 3.9.

Fig. 4(a–d) show the histogram of particle sizes of the compositions. Using ImageJ software the particle size has been calculated from FE-SEM micrographs. The histogram fitted with a Gaussian function shows that BAS exhibits an average particle size of 70 nm, while BAS005 with 88 nm, BAS01 with 102 nm, BAS02 with 118 nm.

3.4 XPS analysis of $BaSn_{1-x}Cu_xO_3$

X-ray photoemission spectroscopy (XPS) was used to examine the oxidation state and surface chemical interactions of pure $BaSnO_3$ and $BaSn_{0.8}Cu_{0.2}O_3$.[56,57] Fig. 5(a) display the XPS Survey spectrum (look similar) of pure BAS and BAS02. The peaks in the spectrum correspond to the elements Ba, Sn, O and Cu elements in the photocatalyst. Fig. 5(b) presents the core-level XPS spectra of Ba, displaying two peaks at 780.6 eV and 795.35 eV for BAS and 780.02 eV and 795.32 eV for BAS02. These peaks correspond to the Ba $3d_{5/2}$ and Ba $3d_{3/2}$ states, respectively,[58] Fig. 5(c) illustrates the Sn 3d spectrum. For BAS, the peaks corresponding to the Sn $3d_{3/2}$ and Sn $3d_{5/2}$ states appear at 486.67 eV and 495.18 eV, respectively, with a peak separation of 8.51 eV. Similarly, for BAS02, the Sn $3d_{3/2}$ and Sn $3d_{5/2}$ peaks are observed at 486.62 eV and 495.08 eV, with a binding energy separation of 8.0 eV. Fig. 5(d) shows the valence band spectrum of BAS and BAS02, revealing a 0.22 eV shift towards the Fermi level, suggesting a significant reduction in the valence band energy Fig. 5(e) present the deconvoluted O 1s spectra of BAS and BAS02 (ref. 59 and 60) and Fig. 5(f) core level splitting of peaks of Cu 2p. The Cu 2p XPS spectrum of BAS02 shows a Cu^{2+} peak at 932.98 eV for the Cu $2p_{3/2}$ state. This is unequivocally confirmed by two characteristic shake-up satellites observed at 942.35 eV and 940.85 eV. These features collectively demonstrate the presence of copper in the +2 oxidation state within the sample. The O 1s spectrum exhibits peaks at 530.9 eV and 530.1 eV, corresponding to lattice oxygen, while a shoulder peak at 533.4 eV and 532.5 eV indicates the presence of hydroxyl groups in the samples. Importantly, an oxygen-vacancy-related peak at 532.6 eV suggests an oxygen vacancy concentration of 27.80% for BAS and 33.8% for BAS02, indicating a higher vacancy level in Cu-doped $BaSnO_3$. The percentage for OL, OV and OC in both BAS and BAS02 are detailed in Table S1.†

3.5 UV-visible spectra of $BaSn_{1-x}Cu_xO_3$

The optical spectrum of the synthesized Cu-doped $BaSnO_3$ was examined by combining UV-vis diffuse reflectance spectroscopy (UV-vis-DRS) and photoluminescence emission spectrum (PL).[61] In the DRS spectra, the absorption edges are in the range of 258–262 nm, Fig. 6. In Fig. 6, the Tauc plot is shown using the Kubelk–Munk method and the band gaps of the system calculated are found to be in the range of 3.15–2.42 eV using the formula, $h\nu = A(h\nu - E_g)n/2$ where α, h, ν, A, and E_g, correspond to the absorption coefficient, Planck's constant, light frequency, a constant, and band gap energy, respectively[62]

3.6 Photoluminescence spectra

As the photoluminescence (PL) of photocatalysts is related to the recombination of photogenerated carriers, PL spectroscopy is often used to evaluate the carrier separation efficiency of photocatalysts The PL spectrum is often used to reveal the separation of electron–hole (e^-/h^+) pairs in semiconductors.[63] Therefore, the PL spectrum of $BaSn_{1-x}Cu_x\ O_3$ is studied and is shown in (Fig. 7).

PL intensity decreases continuously on doing with Cu indicating that the dopant inhibits the recombination process of electron–hole pairs and $x = 0.2$ exhibits the least intensity, hence its photocatalytic activity is highest similar to that observed in doped systems of $SrTiO_3$.[64] The compositions exhibit intense emission around 424 nm corresponding to the inter band transition and peaks in visible region indicating the presence of oxygen vacancies. The emissions at 451, 470, 496 and 550 nm correspond to transitions in the constituent elements as assigned by Payling and Larkins data.[65]

3.7 Photocatalytic activity

Methylene blue dye degradation under UV-visible irradiation is illustrated to demonstrate the photocatalytic activity as followed by the absorption maximum of MB at 663 nm with time control experiment is included in Fig S1.† $BaSnO_3$ shows the lowest photocatalytic activity (Fig. 8) with 92% degradation in 3 h. The photocatalytic activity of $BaSn_{1-x}Cu_xO_3$, where $x = 0.05$, 0.1, and 0.2 increases significantly (Fig. 8) in comparison with that of $BaSnO_3$. It confirms almost the complete degradation of MB dye, as indicated by the decrease in absorption intensities for BAS02 within 30 minutes and the results are tabulated in Table 3. The rate constant increases with increase in Cu substitution and the rate constant of $x = 0.2$ composition is 8 times higher than that of the parent phase. The presence of oxygen vacancies in Cu-doped $BaSnO_3$ is believed to play a crucial role in enhancing the photocatalytic activity. These vacancies act as trapping sites for photogenerated electrons, promoting charge

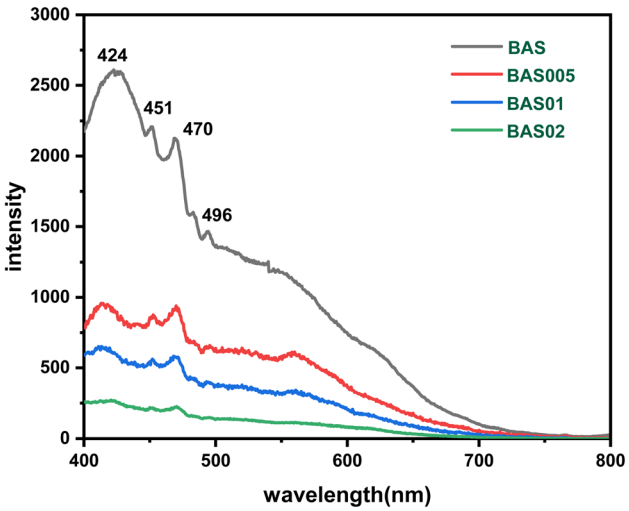

Fig. 7 PL spectra of $BaSn_{1-x}Cu_xO_3$.

separation and facilitating the generation of reactive oxygen species that degrade the MB dye. The effects of catalyst dosage and dye concentration are studied.

3.8 Effect of catalyst dose

The quantity of the catalyst used for the photocatalysis reaction plays a crucial role in determining the efficiency of the reaction

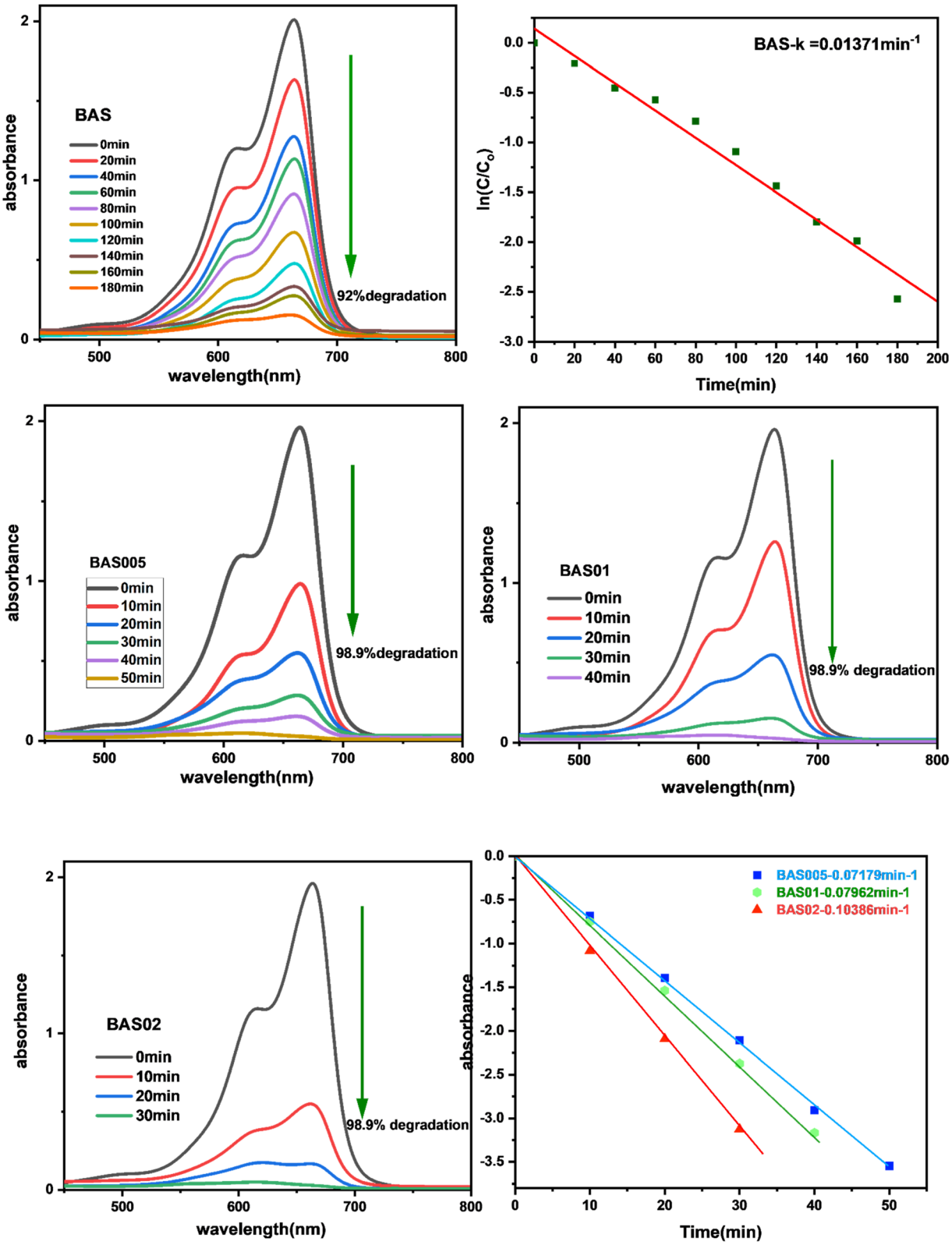

Fig. 8 MB dye degradation and kinetics plot of BAS. MB dye degradation and kinetics plot of BAS005, BAS01, BAS02.

Table 2 The degradation efficiency of $BaSn_{1-x}Cu_xO_3$

Composition	Source	Time (min)	% Of degradation	Rate constant ($\times 10^{-2}$ min^{-1})
BAS	UV	180	92	1.3
BAS005	Visible	50	98.9	7.1
BAS01	Visible	40	98.9	7.9
BAS02	Visible	30	98.9	10.3

as it directly relates to the availability of the active sites. Therefore, the catalyst dose was varied from 20 to 50 mg for the photodegradation of MB and the results are shown in Fig. S2–S4.† It reveals that the BAS02 efficiency increases linearly from 88.8 to 98.9% upon increasing the catalytic dose. Thus 50 mg is fixed as the optimized catalyst dose for further studies. Table S2† depicts a comparison table showing the superior features of the photocatalyst kinetics and dosage compared to literature reports.

3.9 Effect of concentration of pollutant

The concentration of the pollutant directly impacts the overall photocatalytic efficiency of Cu-doped $BaSnO_3$. Generally, an increase in pollutant concentration leads to a decrease in degradation efficiency. To explore this, the pollutant concentration was adjusted from 10 to 30 ppm (as shown in Fig. S4 and S5†), using the optimized catalytic dose of 50 mg. From these observations, it is evident that the Cu-doped $BaSnO_3$ photocatalyst exhibits strong performance up to a pollutant concentration of 10 ppm. Beyond this point, any further increase in pollutant concentration reduces the overall photocatalytic efficiency. Consequently, 10 ppm was established as the optimal concentration for subsequent investigations.

3.10 Photocatalytic activity in sunlight

Solar power is a renewable source of energy which is naturally available and abundant. Hence, sunlight for photocatalysis prominently reduces energy consumption and promotes sustainability. This study examined the sunlight-driven photocatalytic performance of copper-doped catalysts (BAS005, BAS01, BAS02) and compared it to the parent material, BAS. The photocatalytic performance, kinetic profile and percentage degradation are given in (Fig. 9) and the results are tabulated in Table 3. The rate constants increase with increase in Cu substitution. The parent phase degrades the dye to 22% in 3 h whereas the $x = 0.2$ degrades 98% in 30 minutes. The rate constant of $x = 0.2$ composition is 60 times higher than that of the parent phase. It can be attributed to the increase in oxygen vacancies as Cu is substituted and these vacancies act as charge separation centres. Additionally, Table S3† provides a comparison of MB degradation under sunlight to existing literature data.

Table 3 The degradation efficiency of $BaSn_{1-x}Cu_xO_3$ under sunlight

Composition	Source	Time (min)	% Of degradation	Rate constant ($\times 10^{-2}$ min^{-1})
BAS	Sunlight	180	22.2	0.17
BAS005	Sunlight	50	98.9	7.2
BAS01	Sunlight	40	98.9	7.8
BAS02	Sunlight	30	98.9	10.4

3.11 HRMS analysis

High-resolution mass spectrometry (HRMS) provides precise and detailed information about the molecular mass and fragmentation pathways of molecules (Fig. S6–S8†). In the MB degradation process, which occurs through interaction with reactive oxygen species (ROS) generated by the photocatalyst, a total of 16 photo-intermediates were identified using HRMS analysis.[66–68] The plausible degradation mechanism follows three distinct photodegradation pathways, as shown in (Fig. 10). Pathway 1 starts with MB cation (P-1, $m/z = 284$), which undergoes cleavage of one methyl group from the amine, forming PA1 ($m/z = 256$). PA1 then undergoes a ring-opening reaction with ROS, producing several intermediates, including PA2 ($m/z = 141$), PA3 ($m/z = 173$), and PB5 ($m/z = 158$). Pathway 2 begins with the oxidation of the Thio group in MB, forming sulfonic acid PB1 ($m/z = 304$). This is followed by a ring-opening reaction, leading to the formation of PB2 ($m/z = 249$), PB3 ($m/z = 220$), PB4 ($m/z = 186$), and PB5 ($m/z = 158$), which further undergo cleavage in reaction with ROS. In Pathway 3, MB is broken down at both methyl groups, producing intermediates PC1 ($m/z = 258$), PC2 ($m/z = 172$), PC3 ($m/z = 155$), PC4 ($m/z = 128$), PC5 ($m/z = 111$), and PC6 ($m/z = 94$). Ultimately, all the intermediates degrade further into smaller molecules and are eventually eliminated as CO_2 and H_2O over an extended period.

3.12 Photocatalytic mechanism

The general mechanism that generates ROS in sunlight and reaction conditions (visible light) is shown below. Electrons in the valence band are excited to move into the conduction band, creating holes in the VB and electrons in the CB. The dyes may be deteriorated by $^{\bullet}OH$ radicals and superoxide radicals, which are produced when holes and electrons react with water and oxygen, respectively.[69–71]

3.13 Photon absorption

When a photon with sufficient energy strikes the surface of Cu-doped $BaSnO_3$ nanoparticles, it can be absorbed by the semiconductor. This process excites electrons from the valence band (VB) to the conduction band (CB), creating electron–hole pairs. It involves the excitation of electrons from the valence band to the conduction band resulting in holes in VB and electrons in CB. Holes and electrons react with water and oxygen producing $^{\bullet}OH$ radicals and superoxide radicals, respectively that could degrade the dyes. In sunlight and visible light, the mechanism is the usual photocatalytic mechanism as shown in Fig. 11, along with the proposed mechanism.

(1) Light absorption:

$$Cu\text{–}BaSnO_3 + h\nu \rightarrow e^- OH + h^+(VB) \quad (2)$$

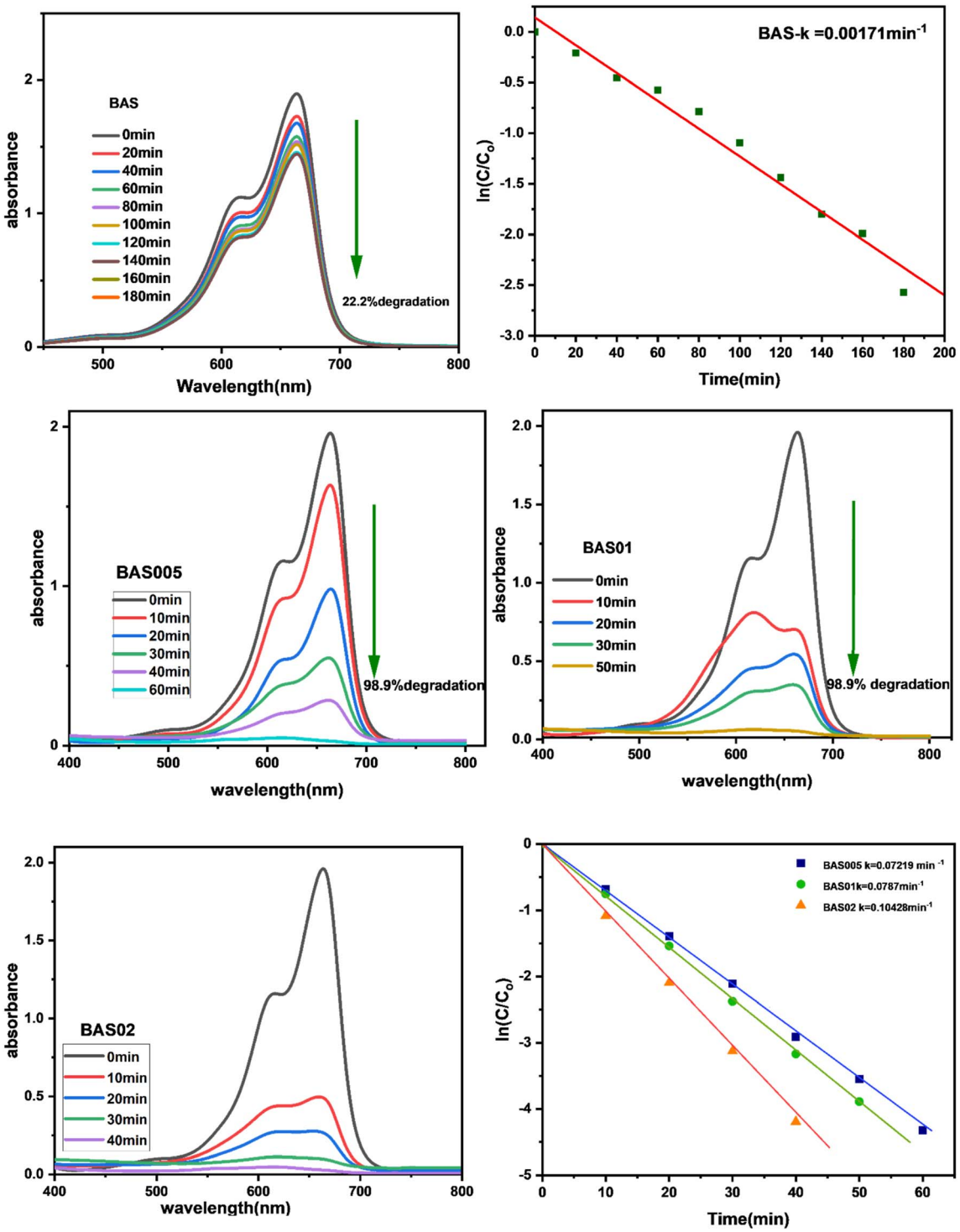

Fig. 9 MB dye degradation of BAS and kinetics plot of BAS under sunlight. Sunlight MB dye degradation and kinetics plot of BAS005, BAS01, BAS02.

(2) Charge separation:

$$e^- + O_2 \rightarrow {}^{\bullet}O_2^- \text{ (superoxide radical)} \quad (3)$$

$$h^+ + H_2O \rightarrow {}^{\bullet}OH \text{ (hydroxyl radical)} \quad (4)$$

Thus, valence band holes react with the chemisorbed H_2O molecules to produce reactive species such as $^{\bullet}OH$ radicals that attack dye molecules, leading to their degradation.

The valence band holes react with the chemisorbed H_2O molecules to produce reactive species such as $^{\bullet}OH$ radicals eqn (5) that attack dye molecules leading to its degradation.

$$H_2O + h^+ \rightarrow {}^{\bullet}OH + H^+ \quad (5)$$

On the other side, e^-(CB) and h^+(VB) can recombine on the surface of the Cu-doped $BaSnO_3$ particle within a short time, and the resulting energy degenerates as heat. Besides, the e^-(CB) and the h^+(VB) can be trapped in surface states, such as Cu vacancies or oxygen vacancies, where they can react with adsorbed species.

The e^-(CB) could react with an acceptor, *e.g.*, dissolved O_2, which consequently is transformed into a superoxide radical anion ($^{\bullet}O_2^-$) leading to the additional formation of $HO_2^{\bullet}$. This process can be represented as

$$e^- (CB) + O_2 \rightarrow {}^{\bullet}O_2^- \quad (6)$$

$$^{\bullet}O_2^- + H^+ \rightarrow HO_2^{\bullet} \quad (7)$$

The hydroperoxide radicals ($HO_2^{\bullet}$) and the hydroxyl radicals ($^{\bullet}OH$) can combine among themselves to form H_2O_2 and O_2 as shown in eqn (6) and (7):

$$HO_2^{\bullet} + {}^{\bullet}OH \rightarrow H_2O_2 + O_2 \quad (8)$$

$$HO_2^{\bullet} + HO_2^{\bullet} \rightarrow H_2O_2 + O_2 \quad (9)$$

H_2O_2 can combine with e^-as given in eqn (10):

$$H_2O_2 + e^- \rightarrow {}^{\bullet}OH + OH^- \quad (10)$$

Cu Doping and Photocatalytic Mechanism:

When divalent Cu is doped into $BaSnO_3$, oxygen vacancies are created, and these can capture holes in the space charge region, forming singly and doubly ionized vacancies, namely, VO^+ and VO^{++}. These levels are present below the CB of Cu-doped $BaSnO_3$.[72] These vacancies can trap the electrons produced by the excitation as per eqn (11) and (12)

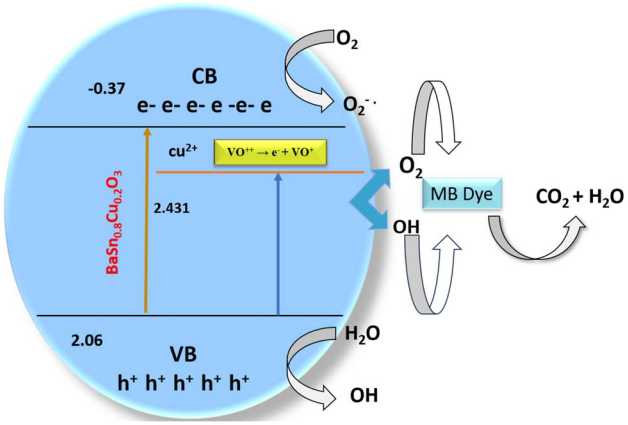

Fig. 11 Proposed band structure and photocatalytic mechanism.

$$h^+ + VO \rightarrow VO^+ \quad (11)$$

$$h^+ + VO^+ \rightarrow VO^{++} \quad (12)$$

These vacancies can ionize later, releasing electrons into the CB as per eqn (13) and (14):

$$VO^+ \rightarrow e^- + VO^{++} \quad (13)$$

$$VO^{++} \rightarrow e^- + VO^+ \quad (14)$$

These electrons migrate to the surface to interact with O_2 to form superoxide radicals as per eqn (15):

$$e^- + O_2 \rightarrow {}^{\bullet}O_2^- \quad (15)$$

$^{\bullet}O_2^- + {}^{\bullet}OH$ + MB dye → degraded MB dye products

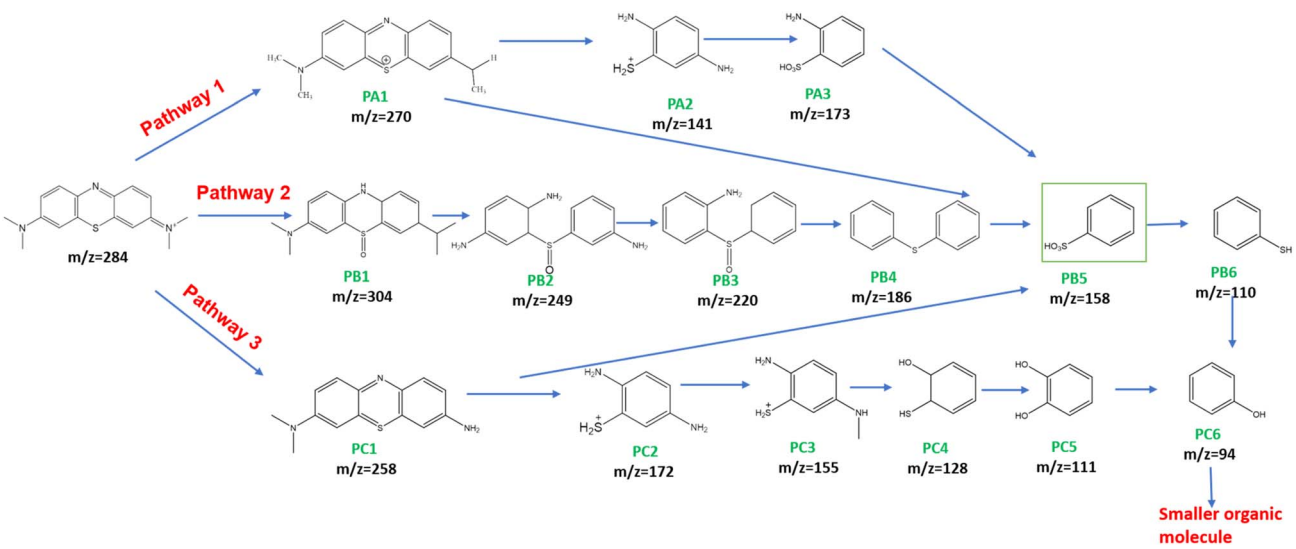

Fig. 10 Proposed possible degradation pathways of Methylene blue.

$$Cu^{+} + O_2 \rightarrow Cu^{2+} + {}^{\bullet}O_2^{-} \quad (16)$$

$${}^{\bullet}O_2^{-} + H^{+} \rightarrow HO_2^{\bullet} \quad (17)$$

$$HO_2^{\bullet} + \text{MB dye} \rightarrow \text{degraded MB dye products}$$

$$\text{MB dye} \rightarrow {}^{\bullet}OH \rightarrow \text{demethylated MB} \rightarrow \text{cleaved MB} \rightarrow CO_2 + H_2O$$

The Cu doping process thus enhances charge carrier separation, preventing recombination, and hence the Cu-doped $BaSnO_3$ acts as a better photocatalyst than $BaSnO_3$.

3.14 Summary of the mechanism

$BaSn_{1-x}Cu_xO_3$ acts as a visible-light-driven photocatalyst. Copper doping enhances both light absorption and charge carrier separation. The resulting hydroxyl and superoxide radicals efficiently degrade methylene blue dye into less harmful products.

4 Reusability studies

After 3 cycles, degradation products were centrifuged, washed with DI water, and dried in the oven at 60 °C. Afterward, the BAS02 photocatalyst was characterized through XRD and IR depicted in the ESI (Fig. S9 and S10).† The XRD patterns indicate that the photocatalyst's crystallinity remains mostly unchanged even after three cycles of use.

From (Fig. S11†), it is observed that the photocatalytic activity was found to be 98.9% (1st cycle), 95.5 (2nd cycle), and 94.2% (3rd cycle) indicating that there is no significant loss in the activity. The above confirms the stability and reusability of BAS02.

5 Conclusion

The $BaSn_{1-x}Cu_xO_3$ was successfully synthesized by a solid-state method. XRD, FTIR, FESEM, XPS, UV, and PL analysis characterized the prepared compounds. In this study, Cu-doped $BaSnO_3$ nanoparticles exhibited enhanced photocatalytic degradation of methylene blue dye under visible and sunlight irradiation. The Cu doping significantly improved the photocatalytic efficiency of $BaSnO_3$, with a degradation rate of 98.9% under visible light and 98.9% under sunlight within 30 minutes. This enhanced performance is likely attributed to the creation of oxygen vacancies due to the copper doping, which facilitates charge separation and improves the overall photocatalytic process. The results highlight the potential of Cu-doped $BaSnO_3$ as a highly efficient and sustainable photocatalyst for dye degradation. These findings contribute to the development of innovative solutions for environmental remediation and pollution control. The excellent photocatalytic activity $BaSn_{0.8}Cu_{0.2}O_3$ for MB degradation under visible light irradiation, likely due to oxygen vacancies, makes them a promising material for environmental remediation applications.

Data availability

The data supporting this article have been included as part of the ESI.†

Author contributions

Methodology, investigation, data curation, formal analysis, writing – original draft, R. S. conceptualization, supervision, visualization, writing – review & editing, funding acquisition, project administration, V. R.

Conflicts of interest

There are no conflicts to declare.

Acknowledgements

The authors thank VIT for providing 'VIT SEED GRANT (RGEMS) – Sanction Order no: SG20230024 for carrying out this research work.

References

1 I. Mondal, P. Halder, A. Chatterjee, N. Bag, S. Sau, S. Biswas, D. Mondal, B. K. Paul, P. K. Paul and S. Das, *J. Environ. Chem. Eng.*, 2024, **12**, 112385.
2 A. Saleem, I. Shahzad, P. Akhter, U. Younas, F. Ali, A. Ahmad, Z. M. El-Bahy, Y. M. Riyad, M. Iqbal and Z. Saeed, *J. Alloys Compd.*, 2025, **1010**, 176922.
3 J. N. Tsaviv, I. S. Eneji, R. Shato'Ato, I. Ahemen, P. R. Jubu and Y. Yusof, *Heliyon*, 2024, **10**, e34517.
4 K. A. B. Beegum, S. Ganesh, C. Sabu, A. S. Varghese, A. S. Aiswarya, C. Thomas, S. Sasi, A. Mathew, A. Jose and R. Raman, *Surf. Interfaces*, 2024, **55**, 105358.
5 A. A. Alothman, N. Ahmad, M. D. Albaqami, Z. A. Alothman, K. N. Alqahtani, M. R. Khan and V. Vasanthakumar, *Ceram. Int.*, 2024, **50**, 15867–15878.
6 D. Deeksha, P. Kour, I. Ahmed, K. K. Haldar, C. S. Yadav, S. K. Sharma and K. Yadav, *J. Alloys Compd.*, 2023, **960**, 171073.
7 J. R. Reddy, S. Kurra, R. Guje, S. Palla, N. K. Veldurthi, G. Ravi and M. Vithal, *Ceram. Int.*, 2015, **41**, 2869–2875.
8 P. Amalthi, J. J. Vijaya, L. J. Kennedy, A. Mustafa and M. Bououdina, *J. Phys. Chem. Solids*, 2022, **169**, 110860.
9 V. Misra, V. Singh, A. Singh, D. Kumar and S. K. Sharma, *Appl. Surf. Sci. Adv.*, 2023, **18**, 100491.
10 I. Shaheen, S. Ata, H. Aslam, H. Farooq, A. Ali, Z. M. Elqahtani, N. Alwadai, M. Iqbal, H. Arif and A. Nazir, *Desalin. Water Treat.*, 2024, **318**, 100389.
11 N. N. Mharsale, P. S. More, Y. B. Khollam, S. F. Shaikh, A. M. Al-Enizi and S. R. Gadakh, *J. Phys. Chem. Solids*, 2024, **192**, 112049.
12 S. Ata, I. Shaheen, H. Aslam, I. U. Mohsin, N. Alwadai, M. Al Huwayz, M. Iqbal and U. Younas, *Results Phys.*, 2023, **49**, 106235.

13 G. Arulprakash and R. Vijayaraghavan, *Appl. Surf. Sci.*, 2025, **684**, 161938.
14 M. Bathwar and R. Vijayaraghavan, *J. Nanopart. Res.*, 2023, **25**, 101534.
15 D. Harikaran and R. Vijayaraghavan, *New J. Chem.*, 2023, **47**, 20733–20743.
16 C. M. Khor, M. M. Khan, M. Y. Khan, A. Khan and M. H. Harunsani, *J. Saudi Chem. Soc.*, 2022, **26**, 101534.
17 S. Gouadria, A. G. Al-Sehemi, S. Manzoor, M. Abdullah, A. Ghafoor Abid, N. Raza, L. V. Panina, M. I. Sayyed, D. I. Tishkevich and A. V. Trukhanov, *J. Photochem. Photobiol., A*, 2024, **448**, 115305.
18 F. M. Sanakousar, C. C. Vidyasagar, D. B. Shikandar, N. Mounesh, C. C. Viswanatha and S. S. Chigari, *React. Chem. Eng.*, 2023, **9**, 388–409.
19 H. Nayak and B. Padhi, *Results Chem.*, 2023, **6**, 101104.
20 H. S. Anusha, S. Yadav, T. Tenzin, J. S. Prabagar, K. M. Anilkumar, W. Kitirote and H. P. Shivaraju, *Int. J. Environ. Sci. Technol.*, 2023, **20**, 13519–13534.
21 W. Zhang, J. Tang and J. Ye, *J. Mater. Res.*, 2007, **22**, 1859–1871.
22 H. Li, Y. Gao, D. Gao and Y. Wang, *Appl. Catal., B*, 2019, **243**, 428–437.
23 S. Upadhyay, O. Parkash and D. Kumar, *Mater. Lett.*, 2001, **49**, 251–255.
24 P. Singh, O. Parkash and D. Kumar, *Solid State Ionics*, 2005, **176**, 2167–2170.
25 K. Balamurugan, N. Harish Kumar, B. Ramachandran, M. S. Ramachandra Rao, J. Arout Chelvane and P. N. Santhosh, *Solid State Commun.*, 2009, **149**, 884–887.
26 S. Lee, H. Wang, P. Gopal, J. Shin, H. M. I. Jaim, X. Zhang, S. Y. Jeong, D. Usanmaz, S. Curtarolo, M. Fornari, M. Buongiorno Nardelli and I. Takeuchi, *Chem. Mater.*, 2017, **29**, 9378–9385.
27 H. Mizoguchi, H. W. Eng and P. M. Woodward, *Inorg. Chem.*, 2004, **43**, 1667–1680.
28 P. H. Borse, U. A. Joshi, S. M. Ji, J. S. Jang, J. S. Lee, E. D. Jeong and H. G. Kim, *Appl. Phys. Lett.*, 2007, **91**, 2430932.
29 M. M. Lee, J. Teuscher, T. Miyasaka, T. N. Murakami and H. J. Snaith, *Science*, 2012, **338**, 643–647.
30 K. F. Moura, L. Chantelle, D. Rosendo, E. Longo and I. M. G. dos Santos, *Mater. Res.*, 2017, **20**, 317–324.
31 S. Chen, R. Liu, Z. Kuai, X. Li, S. Lian, D. Jiang, J. Tang, L. Li, R. Wu and C. Peng, *Environ. Res.*, 2022, **204**, 111949.
32 J. John, S. Suresh, S. Pillai, S. Pillai, R. Philip and V. P. M. Pillai, *J. Mater. Sci.: Mater. Electron.*, 2021, **32**, 11763–11780.
33 S. Bhandari, A. Roy, T. K. Mallick and S. Sundaram, *Chem. Eng. J.*, 2022, **446**, 137378.
34 R. Dileep K, M. K. Rajbhar, A. Ashina, E. Ramasamy, S. Mallick, T. N. Rao and G. Veerappan, *Mater. Chem. Phys.*, 2020, **243**(35), 123939.
35 Q. Ji, L. Bi, J. Zhang, H. Cao and X. S. Zhao, *Energy Environ. Sci.*, 2020, **13**, 1408–1428.
36 L. Hao, H. Huang, Y. Zhang and T. Ma, *Adv. Funct. Mater.*, 2021, **31**, 2100919.
37 L. H. Yang, Z. Q. Lin, M. T. Liao, W. J. Yang, J. X. Pan, W. Li, C. Yang, Y. J. Wu, G. Z. Wang and S. H. Lv, *Appl. Surf. Sci.*, 2023, **621**, 158208.
38 H. Tan, Z. Zhao, W. B. Zhu, E. N. Coker, B. Li, M. Zheng, W. Yu, H. Fan and Z. Sun, *ACS Appl. Mater. Interfaces*, 2014, **6**, 19184–19190.
39 B. Rivas-Murias, J. Rivas and M. A. Senarís-Rodríguez, *J. Alloys Compd.*, 2012, **516**, 113–118.
40 S. S. Li, M. Y. Yan, F. Y. Fan, W. Q. Dong, F. S. Luo, S. J. Zhang, Y. Zhang, L. Chen, J. M. Yan, S. T. Zhang, F. F. Wang and R. K. Zheng, *J. Mater. Sci.: Mater. Electron.*, 2023, **34**, 1–9.
41 B. B. N. Anchal, P. Singh and R. Pyare, *Mater. Today: Proc.*, 2019, **18**, 1310–1316.
42 S. Song, Z. Yang, X. Wang, Y. Bai, S. Qin, Q. Li, M. Xu, S. Yuan and Q. Xu, *J. Supercond. Novel Magn.*, 2022, **35**, 3551–3558.
43 Y. Li, S. Wang, Y. Xia and L. Gao, *New J. Chem.*, 2022, **46**, 5176–5187.
44 F. Granados-Chinchilla and C. Rodríguez, *J. Anal. Methods Chem.*, 2017, **1**, 1315497.
45 K. Pandey, S. Chauhan and M. Kumar, *J. Electron. Mater.*, 2024, **53**, 4782–4789.
46 A. Ammasi, A. P. Munusamy, M. Shkir, B. Vellingiri, V. R. M. Reddy and W. K. Kim, *J. Mater. Sci.: Mater. Electron.*, 2023, **34**, 1–13.
47 B. B. N. Anchal, P. Singh and R. Pyare, *Mater. Today: Proc.*, 2019, **18**, 1310–1316.
48 J. Jeon, Y. Ha, J. L. MacManus-Driscoll and S. Lee, *Nano Convergence*, 2023, **10**, 50.
49 S. S. Li, M. Y. Yan, F. Y. Fan, W. Q. Dong, F. S. Luo, S. J. Zhang, Y. Zhang, L. Chen, J. M. Yan, S. T. Zhang, F. F. Wang and R. K. Zheng, *J. Mater. Sci.: Mater. Electron.*, 2023, **34**, 1–9.
50 M. A. L. Grace, K. V. Rao, K. Anuradha, A. J. Jayarani, A. A. Kumar and A. Rathika, *Mater. Today: Proc.*, 2023, **92**, 1334–1339.
51 S. M. Yakout, H. A. Mousa, H. T. Handal and W. Sharmoukh, *J. Solid State Chem.*, 2020, **281**, 121028.
52 W. Shepherd, M. Wilms, J. van Embden and E. Della Gaspera, *Chem. Commun.*, 2019, **55**, 11880–11883.
53 Y. An, Y. Ren, D. Yang, Z. Wu and J. Liu, *J. Phys. Chem. C*, 2015, **119**, 4414.
54 J. John, S. Suresh, M. Sivakumar and V. P. M. Pillai, *Mater. Lett.*, 2024, **359**, 135957.
55 I. Manzoor and R. Vijayaraghavan, *New J. Chem.*, 2024, **48**, 20126–20139.
56 J. John, S. R. Chalana, R. Prabhu and V. P. Mahadevan Pillai, *Appl. Phys. A: Mater. Sci. Process.*, 2019, **125**, 1–14.
57 X. Chen, Z. Zhang, S. Chen, Q. Dong, *et al.*, *Opt. Mater.*, 2022, **134**, 113202.
58 J. Wang and B. Luo, *Phys. B*, 2021, **601**, 412586.
59 Y. Jayavelu, G. Maharana, D. P. Joseph, S. Divyadharshini, V. Sakthinathan, K. Manavalan, S. Vijayaraghavan and K. Krishnan, *Electrochim. Acta*, 2024, **502**, 144777.
60 F. Liu, J. Qin, J. Sun, Z. Xu, C. Du, Y. Tu and Z. Ren, *Chem. Eng. Sci.*, 2025, **283**, 121179.

61 A. S. Deepa, S. Vidya, P. C. Manu, S. Solomon, A. John and J. K. Thomas, *J. Alloys Compd.*, 2011, **509**, 1830–1835.
62 M. Zeyrek Ongun, S. Oguzlar, S. A. Akalin and S. Yildirim, *J. Mater. Sci.: Mater. Electron.*, 2021, **32**, 15160–15170.
63 T. R. Sobahi and A. Shawky, *Surf. Interfaces*, 2023, **39**, 102979.
64 M. Abdi, V. Mahdikhah and S. Sheibani, *Opt. Mater.*, 2020, **102**, 109803.
65 W. Xiao, Q. Chen, Y. Wu, T. Wu and L. Dai, *Mater. Chem. Phys.*, 2010, **123**, 1–4.
66 M. Cohen, N. Ferroudj, A. Combes, V. Pichon and S. Abramson, *J. Environ. Chem. Eng.*, 2019, **7**, 102987.
67 T. Zhang, T. Oyama, A. Aoshima, H. Hidaka, J. Zhao and N. Serpone, *J. Photochem. Photobiol., A*, 2001, **140**, 163–172.
68 A. Houas, H. Lachheb, M. Ksibi, E. Elaloui, C. Guillard and J.-M. Herrmann, *Appl. Catal., B*, 2001, **31**, 145–157.
69 M. Kandasamy, V. Vasudevan, P. Thangavelu, B. Parasuraman, R. Boddula, R. Pothu, P. Shanmugam and K. Nadesan, *Emergent Mater.*, 2024, **7**, 987–998.
70 S. Al-Yahyaey, H. H. Kyaw, M. T. Z. Myint, R. Al-Hajri, J. Al-Sabahi and M. Al-Abri, *J. Nanopart. Res.*, 2024, **26**, 72.
71 Z. Kalaycıoglu, B. Ozugur Uysal, O. Pekcan and F. B. Erim, *ACS Omega*, 2023, **8**, 13004–13015.
72 Q. Zhang, M. Xu, B. You, Q. Zhang, H. Yuan and K. Ostrikov, *Appl. Sci.*, 2018, **8**, 353.